



## UvA-DARE (Digital Academic Repository)

### Measurement of proton structure function $F_2$ at low $x$ and low $Q^2$ at HERA

Derrick(et al.), M.; Botje, M.A.J.; Chlebana, F.S.; Dake, A.P.; Engelen, J.J.; de Kamps, M.; Kooijman, P.M.; Kruse, A.; Tiecke, H.G.J.M.; Verkerke, W.; Vreeswijk, M.; Wiggers, L.W.; de Wolf, E.; van Woudenberg, R.

**DOI**

[10.1007/s002880050064](https://doi.org/10.1007/s002880050064)

**Publication date**

1996

**Published in**

Zeitschrift für Physik. C, Particles and Fields

[Link to publication](#)

**Citation for published version (APA):**

Derrick(et al.), M., Botje, M. A. J., Chlebana, F. S., Dake, A. P., Engelen, J. J., de Kamps, M., Kooijman, P. M., Kruse, A., Tiecke, H. G. J. M., Verkerke, W., Vreeswijk, M., Wiggers, L. W., de Wolf, E., & van Woudenberg, R. (1996). Measurement of proton structure function  $F_2$  at low  $x$  and low  $Q^2$  at HERA. *Zeitschrift für Physik. C, Particles and Fields*, 69, 607. <https://doi.org/10.1007/s002880050064>

**General rights**

It is not permitted to download or to forward/distribute the text or part of it without the consent of the author(s) and/or copyright holder(s), other than for strictly personal, individual use, unless the work is under an open content license (like Creative Commons).

**Disclaimer/Complaints regulations**

If you believe that digital publication of certain material infringes any of your rights or (privacy) interests, please let the Library know, stating your reasons. In case of a legitimate complaint, the Library will make the material inaccessible and/or remove it from the website. Please Ask the Library: <https://uba.uva.nl/en/contact>, or a letter to: Library of the University of Amsterdam, Secretariat, Singel 425, 1012 WP Amsterdam, The Netherlands. You will be contacted as soon as possible.

UvA-DARE is a service provided by the library of the University of Amsterdam (<https://dare.uva.nl>)

# Measurement of the proton structure function $F_2$ at low $x$ and low $Q^2$ at HERA

ZEUS Collaboration

M. Derrick, D. Krakauer, S. Magill, D. Mikunas, B. Musgrave, J. Repond, R. Stanek, R.L. Talaga, H. Zhang  
Argonne National Laboratory, Argonne, IL, USA <sup>P</sup>

G. Bari, M. Basile, L. Bellagamba, D. Boscherini, A. Bruni, G. Bruni, P. Bruni, G. Cara Romeo, G. Castellini<sup>1</sup>, M. Chiarini, L. Cifarelli<sup>2</sup>, F. Cindolo, A. Contin, M. Corradi, I. Gialas<sup>3</sup>, P. Giusti, G. Iacobucci, G. Laurenti, G. Levi, A. Margotti, T. Massam, R. Nania, C. Nemoz, F. Palmonari, A. Polini, G. Sartorelli, R. Timellini, Y. Zamora Garcia<sup>4</sup>, A. Zichichi  
University and INFN Bologna, Bologna, Italy <sup>f</sup>

A. Bornheim, J. Crittenden, K. Desch, B. Diekmann<sup>5</sup>, T. Doeker, M. Eckert, L. Feld, A. Frey, M. Geerts, M. Grothe, H. Hartmann, K. Heinloth, L. Heinz, E. Hilger, H.-P. Jakob, U.F. Katz, S. Mengel, J. Mollen<sup>6</sup>, E. Paul, M. Pfeiffer, Ch. Rembser, D. Schramm, J. Stamm, R. Wedemeyer  
Physikalisches Institut der Universität Bonn, Bonn, Germany <sup>c</sup>

S. Campbell-Robson, A. Cassidy, W.N. Cottingham, N. Dyce, B. Foster, S. George, M.E. Hayes, G.P. Heath, H.F. Heath, C.J.S. Morgado, J.A. O'Mara, D. Piccioni, D.G. Roff, R.J. Tapper, R. Yoshida  
H.H. Wills Physics Laboratory, University of Bristol, Bristol, U.K. <sup>o</sup>

R.R. Rau

Brookhaven National Laboratory, Upton, L.I., USA <sup>P</sup>

M. Arneodo<sup>7</sup>, R. Ayad, M. Capua, A. Garfagnini, L. Iannotti, M. Schioppa, G. Susinno  
Calabria University, Physics Dept. and INFN, Cosenza, Italy <sup>f</sup>

A. Bernstein, A. Caldwell<sup>8</sup>, N. Cartiglia, J.A. Parsons, S. Ritz<sup>9</sup>, F. Sciulli, P.B. Straub, L. Wai, S. Yang, Q. Zhu  
Columbia University, Nevis Labs., Irvington on Hudson, N.Y., USA <sup>q</sup>

P. Borzemeski, J. Chwastowski, A. Eskreys, K. Piotrkowski, M. Zachara, L. Zawiejski  
Inst. of Nuclear Physics, Cracow, Poland <sup>j</sup>

L. Adamczyk, B. Bednarek, K. Jeleń, D. Kisielewska, T. Kowalski, M. Przybycień, E. Rulikowska-Zarebska, L. Suszycki, J. Zając  
Faculty of Physics and Nuclear Techniques, Academy of Mining and Metallurgy, Cracow, Poland <sup>j</sup>

A. Kotański

Jagellonian Univ., Dept. of Physics, Cracow, Poland <sup>k</sup>

L.A.T. Bauerdick, U. Behrens, H. Beier, J.K. Bienlein, C. Coldewey, O. Deppe, K. Desler, G. Drews, M. Flasiński<sup>10</sup>, D.J. Gilkinson, C. Glasman, P. Göttlicher, J. Große-Knetter, B. Gutjahr<sup>11</sup>, T. Haas, W. Hain, D. Hasell, H. Heßling, Y. Iga, K.F. Johnson<sup>12</sup>, P. Joos, M. Kasemann, R. Klanner, W. Koch, L. Köpke<sup>13</sup>, U. Kötz, H. Kowalski, J. Labs, A. Ladage, B. Löhr, M. Löwe, D. Lüke, J. Mainusch<sup>14</sup>, O. Mańczak, T. Monteiro<sup>15</sup>, J.S.T. Ng, S. Nickel<sup>16</sup>, D. Notz, K. Ohrenberg, M. Roco, M. Rohde, J. Roldán, U. Schneekloth, W. Schulz, F. Selonke, E. Stiliaris<sup>17</sup>, B. Surrow, T. Voß, D. Westphal, G. Wolf, C. Youngman, W. Zeuner, J.F. Zhou<sup>18</sup>  
Deutsches Elektronen-Synchrotron DESY, Hamburg, Germany

H.J. Grabosch, A. Kharchilava<sup>19</sup>, A. Leich, S.M. Mari<sup>3</sup>, M.C.K. Mattingly<sup>20</sup>, A. Meyer, S. Schlenstedt, N. Wulff  
DESY-Zeuthen, Inst. für Hochenergiephysik, Zeuthen, Germany

G. Barbagli, E. Gallo, P. Pelfer  
University and INFN, Florence, Italy <sup>f</sup>

G. Anzivino, G. Maccarrone, S. De Pasquale, L. Votano  
INFN, Laboratori Nazionali di Frascati, Frascati, Italy <sup>f</sup>

A. Bamberger, S. Eisenhardt, A. Freidhof, S. Söldner-Rembold<sup>21</sup>, J. Schroeder<sup>22</sup>, T. Trefzger  
Fakultät für Physik der Universität Freiburg i.Br., Freiburg i.Br., Germany <sup>c</sup>

N.H. Brook, P.J. Bussey, A.T. Doyle, D.H. Saxon, M.L. Utley, A.S. Wilson

Dept. of Physics and Astronomy, University of Glasgow, Glasgow, U.K. <sup>o</sup>

A. Dannemann, U. Holm, D. Horstmann, T. Neumann, R. Sinkus, K. Wick

Hamburg University, I. Institute of Exp. Physics, Hamburg, Germany <sup>c</sup>

E. Badura<sup>23</sup>, B.D. Burow<sup>24</sup>, L. Hagge<sup>14</sup>, E. Lohrmann, J. Milewski, M. Nakahata<sup>25</sup>, N. Pavel, G. Poelz, W. Schott, F. Zetsche

Hamburg University, II. Institute of Exp. Physics, Hamburg, Germany <sup>c</sup>

T.C. Bacon, N. Bruemmer, I. Butterworth, V.L. Harris, B.Y.H. Hung, K.R. Long, D.B. Miller, P.P.O. Morawitz, A. Prinias, J.K. Sedgbeer, A.F. Whitfield

Imperial College London, High Energy Nuclear Physics Group, London, U.K. <sup>o</sup>

U. Mallik, E. McCliment, M.Z. Wang, S.M. Wang, J.T. Wu

University of Iowa, Physics and Astronomy Dept., Iowa City, USA <sup>p</sup>

P. Cloth, D. Filges

Forschungszentrum Jülich, Institut für Kernphysik, Jülich, Germany

S.H. An, S.M. Hong, S.W. Nam, S.K. Park, M.H. Suh, S.H. Yon

Korea University, Seoul, Korea <sup>h</sup>

R. Imlay, S. Kartik, H.-J. Kim, R.R. McNeil, W. Metcalf, V.K. Nadendla

Louisiana State University, Dept. of Physics and Astronomy, Baton Rouge, LA, USA <sup>p</sup>

F. Barreiro<sup>26</sup>, G. Cases, J.P. Fernandez, R. Graciani, J.M. Hernández, L. Hervás<sup>26</sup>, L. Labarga<sup>26</sup>, M. Martinez, J. del Peso, J. Puga, J. Terron, J.F. de Trocóniz

Univer. Autónoma Madrid, Depto de Física Teórica, Madrid, Spain <sup>n</sup>

G.R. Smith

University of Manitoba, Dept. of Physics, Winnipeg, Manitoba, Canada <sup>a</sup>

F. Corriveau, D.S. Hanna, J. Hartmann, L.W. Hung, J.N. Lim, C.G. Matthews, P.M. Patel, L.E. Sinclair, D.G. Stairs, M. St-Laurent, R. Ullmann, G. Zacek

McGill University, Dept. of Physics, Montréal, Québec, Canada <sup>a, b</sup>

V. Bashkirov, B.A. Dolgoshein, A. Stifutkin

Moscow Engineering Physics Institute, Moscow, Russia <sup>1</sup>

G.L. Bashindzhagyan<sup>27</sup>, P.F. Ermolov, L.K. Gladilin, Yu.A. Golubkov, V.D. Kobrin, I.A. Korzhavina, V.A. Kuzmin, O.Yu. Lukina, A.S. Proskuryakov, A.A. Savin, L.M. Shcheglova, A.N. Solomin, N.P. Zotov Moscow State University, Institute of Nuclear Physics, Moscow, Russia <sup>m</sup>

M. Botje, F. Chlebana, A. Dake, J. Engelen, M. de Kamps, P. Kooijman, A. Kruse, H. Tiecke, W. Verkerke, M. Vreeswijk, L. Wiggers, E. de Wolf, R. van Woudenberg<sup>28</sup>

NIKHEF and University of Amsterdam, Netherlands <sup>i</sup>

D. Acosta, B. Bylsma, L.S. Durkin, J. Gilmore, K. Honscheid, C. Li, T.Y. Ling, K.W. McLean<sup>29</sup>, P. Nylander, I.H. Park, T.A. Romanowski<sup>30</sup>, R. Seidlein<sup>31</sup>

Ohio State University, Physics Department, Columbus, Ohio, USA <sup>p</sup>

D.S. Bailey, A. Byrne<sup>32</sup>, R.J. Cashmore, A.M. Cooper-Sarkar, R.C.E. Devenish, N. Harnew, M. Lancaster, L. Lindemann<sup>3</sup>, J.D. McFall, C. Nath, V.A. Noyes, A. Quadt, J.R. Tickner, H. Uijterwaal, R. Walczak, D.S. Waters, F.F. Wilson, T. Yip

Department of Physics, University of Oxford, Oxford, U.K. <sup>o</sup>

G. Abbiendi, A. Bertolin, R. Brugnera, R. Carlin, F. Dal Corso, M. De Giorgi, U. Dosselli, S. Limentani, M. Morandin, M. Posocco, L. Stanco, R. Stroili, C. Voci

Dipartimento di Fisica dell' Università and INFN, Padova, Italy <sup>f</sup>

J. Bulmahn, J.M. Butterworth, R.G. Feild, B.Y. Oh, J.R. Okrasinski<sup>33</sup>, J.J. Whitmore

Pennsylvania State University, Dept. of Physics, University Park, PA, USA <sup>q</sup>

G. D'Agostini, G. Marini, A. Nigro, E. Tassi

Dipartimento di Fisica, Univ. 'La Sapienza' and INFN, Rome, Italy <sup>f</sup>

J.C. Hart, N.A. McCubbin, K. Prytz, T.P. Shah, T.L. Short

Rutherford Appleton Laboratory, Chilton, Didcot, Oxon, U.K. <sup>o</sup>

E. Barberis, T. Dubbs, C. Heusch, M. Van Hook, W. Lockman, J.T. Rahn, H.F.-W. Sadrozinski, A. Seiden, D.C. Williams

University of California, Santa Cruz, CA, USA <sup>p</sup>

J. Biltzinger, R.J. Seifert, O. Schwarzer, A.H. Walenta, G. Zech

Fachbereich Physik der Universität-Gesamthochschule Siegen, Germany <sup>c</sup>

H. Abramowicz, G. Briskin, S. Dagan<sup>34</sup>, C. Händel-Pikielny, A. Levy<sup>27</sup>

School of Physics, Tel-Aviv University, Tel Aviv, Israel <sup>e</sup>

J.I. Fleck, T. Hasegawa, M. Hazumi, T. Ishii, M. Kuze, S. Mine, Y. Nagasawa, M. Nakao, I. Suzuki, K. Tokushuku, S. Yamada, Y. Yamazaki

Institute for Nuclear Study, University of Tokyo, Tokyo, Japan <sup>g</sup>

M. Chiba, R. Hamatsu, T. Hirose, K. Homma, S. Kitamura, Y. Nakamitsu, K. Yamauchi

Tokyo Metropolitan University, Dept. of Physics, Tokyo, Japan <sup>g</sup>

R. Cirio, M. Costa, M.I. Ferrero, L. Lamberti, S. Maselli, C. Peroni, R. Sacchi, A. Solano, A. Staiano

Universita di Torino, Dipartimento di Fisica Sperimentale and INFN, Torino, Italy <sup>f</sup>

M. Dardo

II Faculty of Sciences, Torino University and INFN - Alessandria, Italy <sup>f</sup>

D.C. Bailey, D. Bandyopadhyay, F. Benard, M. Brkic, D.M. Gingrich<sup>35</sup>, G.F. Hartner, K.K. Joo, G.M. Levman, J.F. Martin, R.S. Orr, S. Polenz, C.R. Sampson, R.J. Teuscher

University of Toronto, Dept. of Physics, Toronto, Ont., Canada <sup>a</sup>

C.D. Catterall, T.W. Jones, P.B. Kaziewicz, J.B. Lane, R.L. Saunders, J. Shulman

University College London, Physics and Astronomy Dept., London, U.K. <sup>o</sup>

K. Blankenship, B. Lu, L.W. Mo

Virginia Polytechnic Inst. and State University, Physics Dept., Blacksburg, VA, USA <sup>q</sup>

W. Bogusz, K. Charchuła, J. Ciborowski, J. Gajewski, G. Grzelak<sup>36</sup>, M. Kasprzak, M. Krzyżanowski,

K. Muchorowski<sup>37</sup>, R.J. Nowak, J.M. Pawlak, T. Tymieniecka, A.K. Wróblewski, J.A. Zakrzewski, A.F. Żarnecki

Warsaw University, Institute of Experimental Physics, Warsaw, Poland <sup>j</sup>

M. Adamus

Institute for Nuclear Studies, Warsaw, Poland <sup>j</sup>

Y. Eisenberg<sup>34</sup>, U. Karshon<sup>34</sup>, D. Revel<sup>34</sup>, D. Zer-Zion

Weizmann Institute, Particle Physics Dept., Rehovot, Israel <sup>d</sup>

I. Ali, W.F. Badgett, B. Behrens<sup>38</sup>, S. Dasu, C. Fordham, C. Foudas, A. Goussiou<sup>39</sup>, R.J. Loveless, D.D. Reeder, S. Silverstein, W.H. Smith, A. Vaiciulis, M. Wodarczyk

University of Wisconsin, Dept. of Physics, Madison, WI, USA <sup>p</sup>

T. Tsurugai

Meiji Gakuin University, Faculty of General Education, Yokohama, Japan

S. Bhadra, M.L. Cardy, C.-P. Fagerstroem, W.R. Frisken, K.M. Furutani, M. Khakzad, W.N. Murray, W.B. Schmidke

York University, Dept. of Physics, North York, Ont., Canada <sup>a</sup>

Received: 24 October 1995

---

<sup>1</sup> also at IROE Florence, Italy  
<sup>2</sup> now at Univ. of Salerno and INFN Napoli, Italy  
<sup>3</sup> supported by EU HCM contract ERB-CHRX-CT93-0376  
<sup>4</sup> supported by Worldlab, Lausanne, Switzerland  
<sup>5</sup> now a self-employed consultant  
<sup>6</sup> now at ELEKLUFT, Bonn  
<sup>7</sup> now also at University of Torino  
<sup>8</sup> Alexander von Humboldt Fellow  
<sup>9</sup> Alfred P. Sloan Foundation Fellow  
<sup>10</sup> now at Inst. of Computer Science, Jagellonian Univ., Cracow  
<sup>11</sup> now at Comma-Soft, Bonn  
<sup>12</sup> visitor from Florida State University

---

<sup>13</sup> now at Univ. of Mainz  
<sup>14</sup> now at DESY Computer Center  
<sup>15</sup> supported by European Community Program PRAXIS XXI  
<sup>16</sup> now at Dr. Seidel Informationssysteme, Frankfurt/M.  
<sup>17</sup> now at Inst. of Accelerating Systems & Applications (IASA), Athens  
<sup>18</sup> now at Mercer Management Consulting, Munich  
<sup>19</sup> now at Univ. de Strasbourg  
<sup>20</sup> now at Andrews University, Barrien Springs, U.S.A.  
<sup>21</sup> now with OPAL Collaboration, Faculty of Physics at Univ. of Freiburg  
<sup>22</sup> now at SAS-Institut GmbH, Heidelberg  
<sup>23</sup> now at GSI Darmstadt  
<sup>24</sup> also supported by NSERC

**Abstract.** We report on a measurement of the proton structure function  $F_2$  in the range  $3.5 \times 10^{-5} \leq x \leq 4 \times 10^{-3}$  and  $1.5 \text{ GeV}^2 \leq Q^2 \leq 15 \text{ GeV}^2$  at the  $ep$  collider HERA operating at a centre-of-mass energy of  $\sqrt{s} = 300 \text{ GeV}$ . The rise of  $F_2$  with decreasing  $x$  observed in the previous HERA measurements persists in this lower  $x$  and  $Q^2$  range. The  $Q^2$  evolution of  $F_2$ , even at the lowest  $Q^2$  and  $x$  measured, is consistent with perturbative QCD.

## 1 Introduction

The measurement of deep inelastic scattering (DIS),  $ep \rightarrow eX$ , at HERA has shown a rapid rise of the proton structure function  $F_2(x, Q^2)$  with decreasing  $x$  for  $x \leq 10^{-2}$  [1, 2].

<sup>25</sup> now at Institute for Cosmic Ray Research, University of Tokyo

<sup>26</sup> partially supported by CAM

<sup>27</sup> partially supported by DESY

<sup>28</sup> now at Philips Natlab, Eindhoven, NL

<sup>29</sup> now at Carleton University, Ottawa, Canada

<sup>30</sup> now at Department of Energy, Washington

<sup>31</sup> now at HEP Div., Argonne National Lab., Argonne, IL, USA

<sup>32</sup> now at Oxford Magnet Technology, Eynsham, Oxon

<sup>33</sup> in part supported by Argonne National Laboratory

<sup>34</sup> supported by a MINERVA Fellowship

<sup>35</sup> now at Centre for Subatomic Research, Univ. of Alberta, Canada and TRIUMF, Vancouver, Canada

<sup>36</sup> supported by the Polish State Committee for Scientific Research, grant No. 2P03B09308

<sup>37</sup> supported by the Polish State Committee for Scientific Research, grant No. 2P03B09208

<sup>38</sup> now at University of Colorado, U.S.A.

<sup>39</sup> now at High Energy Group of State University of New York, Stony Brook, N.Y.

<sup>a</sup> supported by the Natural Sciences and Engineering Research Council of Canada (NSERC)

<sup>b</sup> supported by the FCAR of Québec, Canada

<sup>c</sup> supported by the German Federal Ministry for Education and Science, Research and Technology (BMBF), under contract numbers 056BN19I, 056FR19P, 056HH19I, 056HH29I, 056SI79I

<sup>d</sup> supported by the MINERVA Gesellschaft für Forschung GmbH, and by the Israel Academy of Science

<sup>e</sup> supported by the German Israeli Foundation, and by the Israel Academy of Science

<sup>f</sup> supported by the Italian National Institute for Nuclear Physics (INFN)

<sup>g</sup> supported by the Japanese Ministry of Education, Science and Culture (the Monbusho) and its grants for Scientific Research

<sup>h</sup> supported by the Korean Ministry of Education and Korea Science and Engineering Foundation

<sup>i</sup> supported by the Netherlands Foundation for Research on Matter (FOM)

<sup>j</sup> supported by the Polish State Committee for Scientific Research, grants No. 115/E-343/SPUB/P03/109/95, 2P03B 244 08p02, p03, p04 and p05, and the Foundation for Polish-German Collaboration (proj. No. 506/92)

<sup>k</sup> supported by the Polish State Committee for Scientific Research (grant No. 2 P03B 083 08)

<sup>l</sup> partially supported by the German Federal Ministry for Education and Science, Research and Technology (BMBF)

<sup>m</sup> supported by the German Federal Ministry for Education and Science, Research and Technology (BMBF), and the Fund of Fundamental Research of Russian Ministry of Science and Education and by INTAS-Grant No. 93-63

<sup>n</sup> supported by the Spanish Ministry of Education and Science through funds provided by CICYT

<sup>o</sup> supported by the Particle Physics and Astronomy Research Council

<sup>p</sup> supported by the US Department of Energy

<sup>q</sup> supported by the US National Science Foundation

The corresponding increase of the virtual photon-proton cross section  $\sigma_{tot}^{\gamma^*p}$  with the centre-of-mass energy  $W$  is much stronger than that of  $\sigma_{tot}^{\gamma p}$  for real photons [3, 4]. The slower increase of the real photoproduction cross section is consistent with the energy behaviour of hadron-hadron total cross sections. In perturbative QCD the rise of  $F_2$  at low  $x$  is ascribed to an increase in the sea quark density [5, 6], and the significance thereof is discussed extensively in the literature [7]. One of the important questions is how far perturbative QCD retains its validity as one probes large parton densities. Until now the HERA measurements of  $F_2$  have covered  $Q^2$  values above  $4.5 \text{ GeV}^2$ . It is of great interest to extend the  $F_2$  measurement to lower  $Q^2$  values and study the low  $x$  behaviour in the transition region between photoproduction and DIS.

In this paper,  $F_2$  measurements, from  $e^+p$  DIS data, at  $x \geq 3.5 \times 10^{-5}$  and at  $Q^2$  values as low as  $1.5 \text{ GeV}^2$  are reported. Access to such low  $Q^2$  values is achieved in two different ways. For the first analysis (SVX) HERA is operated with the interaction point shifted in the proton direction in order to improve the acceptance for small positron scattering angles. The second analysis (ISR) uses DIS events from the nominal interaction point with initial state photon radiation where the radiated photon is detected. These events effectively have a lower initial positron beam energy and thus for a fixed acceptance of the positron scattering angle events with smaller values of  $Q^2$  can be reconstructed. The reconstruction of events having positrons scattered at small angles is improved compared to the 1993 analysis by the addition of the small angle rear tracking detector (SRTD).

## 2 Experimental conditions

### 2.1 HERA running conditions

The data were taken with the ZEUS detector at HERA in 1994. HERA operated with 153 colliding bunches of 820 GeV protons and 27.5 GeV positrons. Additional unpaired positron and proton bunches circulated, which are used to determine beam related background. The root mean square of the proton bunch length was approximately 20 cm while the positron bunch length was negligible in comparison, leading to an interaction length having a root mean square of 10 cm. For the SVX analysis, the mean interaction vertex was moved from  $Z = 0$  to  $Z = 67 \text{ cm}$ <sup>1</sup>. Approximately 5% of the proton current was contained in satellite bunches, which were shifted by 4.8 ns with respect to the primary bunch crossing time, resulting in a fraction of the  $ep$  interactions occurring on average +72 cm upstream of the primary position.

The SVX analysis is based on an integrated luminosity of  $58 \text{ nb}^{-1}$  collected while HERA operated with the shifted interaction point. The ISR analysis uses  $2.5 \text{ pb}^{-1}$  of data taken with HERA operating with the interaction point at the nominal position,  $Z = 0$ .

<sup>1</sup> The ZEUS coordinate system is defined as right handed with the  $Z$  axis pointing in the proton beam direction, and the  $X$  axis horizontal, pointing towards the centre of HERA. The origin is at the nominal interaction point

## 2.2 The ZEUS detector

A description of the ZEUS detector can be found in [3, 8]. The primary components used in these analyses are the uranium-scintillator calorimeter (CAL) [9] and the tracking detectors. The calorimeter covers 99.7% of the total solid angle and is subdivided into electromagnetic (EMC) and hadronic (HAC) sections with typical cell sizes of  $5 \times 20 \text{ cm}^2$  ( $10 \times 20 \text{ cm}^2$  in the rear calorimeter (RCAL), i.e. in the positron beam direction) and  $20 \times 20 \text{ cm}^2$  respectively. The calorimeter has an energy resolution of  $\sigma/E = 18\%/\sqrt{E(\text{GeV})}$  for electrons and  $\sigma/E = 35\%/\sqrt{E(\text{GeV})}$  for hadrons, as measured in test beams. The timing resolution of a calorimeter cell is better than  $\sigma_t = 1.5/\sqrt{E(\text{GeV})} \oplus 0.5 \text{ ns}$  ( $\oplus$  denotes addition in quadrature).

The tracking system consists of a vertex detector (VXD) [10] and a central tracking chamber (CTD) [11] enclosed in a 1.43 T solenoidal magnetic field. The interaction vertex is measured with a resolution along (transverse to) the beam direction of 0.4 (0.1) cm.

The position of positrons scattered close to the positron beam direction is determined by the SRTD which is attached to the front face of the RCAL. The SRTD consists of two planes of scintillator strips, 1 cm wide and 0.5 cm thick, arranged in orthogonal directions and read out via optical fibres and photomultiplier tubes. It covers the region of  $68 \times 68 \text{ cm}^2$  in  $X$  and  $Y$  and is positioned at  $Z = -148 \text{ cm}$ . A hole of  $20 \times 20 \text{ cm}^2$  at the centre of the RCAL and SRTD accommodates the beampipe. The SRTD is able to clearly resolve single minimum ionising particles (mip) and has a position resolution of 0.3 cm. The time resolution is better than 2 ns for a minimum ionising particle.

The luminosity is measured via the positron-proton bremsstrahlung process,  $ep \rightarrow e\gamma p$ , using a lead-scintillator calorimeter (LUMI) [12] which accepts photons at angles  $\leq 0.5 \text{ mrad}$  with respect to the beam axis. The LUMI photon calorimeter is also used to measure the energy and position of photons from initial state radiation in DIS events. It is positioned at  $Z = -107 \text{ m}$  and, under test beam conditions, has an energy resolution of  $\sigma/E = 18\%/\sqrt{E(\text{GeV})}$ . In its operating position it is shielded from synchrotron radiation by a carbon-lead filter and has an energy resolution of  $\sigma/E = 26.5\%/\sqrt{E(\text{GeV})}$ , as determined from bremsstrahlung data. The position resolution is 0.2 cm. In addition, an electromagnetic calorimeter positioned at  $Z = -35 \text{ m}$  is used for tagging scattered positrons at small angles.

## 2.3 Triggering

Events were filtered online by a three level trigger system [8]. At the first level, DIS events were selected by requiring a logical AND between two conditions based on energy deposits in the calorimeter. The first condition was the presence of an isolated electromagnetic energy deposit. The EMC energy deposit was required to be greater than 2.5 GeV. The corresponding HAC energy deposit was required to be either less than 0.95 GeV or no more than a third of the EMC energy deposit. The threshold values have been chosen to give  $>99\%$  efficiency for positrons with energy greater than 5 GeV as determined by Monte Carlo studies.

Further details of the algorithm can be found in [13]. The second condition required that the EMC section have an energy deposit greater than 3.75 GeV. Background from protons interacting outside the detector was rejected using the time measurement of the energy deposits from downstream veto counters and the SRTD.

At the second level trigger (SLT), background was further reduced using the measured times of energy deposits and the summed energies from the calorimeter. The events were accepted if

$$\delta_{SLT} \equiv \sum_i E_i(1 - \cos \theta_i) > 24 \text{ GeV} - 2E_\gamma \quad (1)$$

where  $E_i$  and  $\theta_i$  are the energies and polar angles (with respect to the primary vertex position) of calorimeter cells, and  $E_\gamma$  is the energy deposit measured in the LUMI photon calorimeter. For perfect detector resolution and acceptance,  $\delta_{SLT}$  is twice the positron beam energy (55 GeV) for DIS events while for photoproduction events, where the scattered positron escapes down the beampipe,  $\delta_{SLT}$  peaks at much lower values.

The full event information was available at the third level trigger (TLT). Tighter timing cuts as well as algorithms to remove beam-halo muons and cosmic muons were applied. The quantity  $\delta_{TLT}$  was determined in the same manner as for  $\delta_{SLT}$ . The events were required to have

$$\delta_{TLT} > 25 \text{ GeV} - 2E_\gamma. \quad (2)$$

Finally, DIS events were accepted if a scattered positron candidate of energy greater than 4 GeV was found.

## 3 Monte Carlo simulation

Monte Carlo (MC) event simulation is used to correct for detector acceptance and smearing effects. The detector simulation is based on the GEANT programme [14] and incorporates our understanding of the detector, the trigger and test beam results. Neutral current DIS events are simulated to  $\mathcal{O}(\alpha_s)$  using the HERACLES programme [15] which includes first order electroweak radiative corrections. The hadronic final state is simulated using the colour-dipole model including boson gluon fusion CDMBGF [16] as implemented in ARIADNE [17] for the QCD cascade and JETSET [18] for the hadronisation. The ARIADNE model currently provides the best description of the observed DIS non-diffractive hadronic final state [19]. Diffractive events with a large rapidity gap as observed in the data [20] are simulated within ARIADNE by assuming that the struck quark belongs to a colourless state having only a small fraction of the proton's momentum. The parameters of the model are adjusted to be consistent with recent ZEUS measurements [21]. The MRSA [22] parton density parameterisations, modified at low  $Q^2$  as described in [23], are used. These parameterisations provide an adequate description of previous ZEUS and H1 measurements [1, 2].

The shape of the vertex distribution used in the simulation is taken from nondiffractive photoproduction events. For such events the vertex reconstruction efficiency is found to be high and only weakly dependent on the  $Z$  position of the interaction.

For the shifted vertex analysis, a sample of events corresponding to an integrated luminosity of  $\sim 100 \text{ nb}^{-1}$  was generated with  $Q^2 > 0.5 \text{ GeV}^2$ .

The main source of background in the data sample for the SVX analysis is due to photoproduction leading to the detection of a fake scattered positron. Minimum bias photoproduction events are simulated using PYTHIA [24] with cross sections according to the ALLM parameterisation [25]. Photoproduction events corresponding to an integrated luminosity of  $110 \text{ nb}^{-1}$  were generated with a photon-proton centre-of-mass energy  $W \gtrsim 190 \text{ GeV}$ . Events with smaller  $W$  values do not contribute to the photoproduction background.

For the ISR analysis, a DIS sample corresponding to an integrated luminosity of  $2.7 \text{ pb}^{-1}$ , with an initial state photon energy above  $3 \text{ GeV}$ , was generated with  $Q^2 > 0.5 \text{ GeV}^2$ .

## 4 Kinematic reconstruction

In deep inelastic scattering,  $e(k)+p(P) \rightarrow e(k')+X$ , the proton structure functions are expressed in terms of the negative of the four-momentum transfer squared,  $Q^2$ , and Bjorken  $x$ . In the absence of QED radiation,

$$Q^2 = -q^2 = -(k - k')^2, \quad (3)$$

$$x = \frac{Q^2}{2P \cdot q}, \quad (4)$$

where  $k$  and  $P$  are the four-momenta of the incoming particles and  $k'$  is the four-momentum of the scattered lepton. The square of the centre-of-mass energy is denoted by  $s$ . The fractional energy transferred to the proton in its rest frame is  $y = Q^2/(sx)$ .

In the SVX analysis,  $Q^2$  and  $x$  are reconstructed from the measured energy,  $E'_e$ , and scattering angle,  $\theta_e$  of the positron,

$$Q_e^2 = 4E_e E'_e \cos^2(\theta_e/2), \quad (5)$$

$$x_e = \frac{E_e E'_e \cos^2(\theta_e/2)}{E_p (E_e - E'_e \sin^2(\theta_e/2))}, \quad (6)$$

where  $E_e$  and  $E_p$  are the positron and proton beam energies and the scattered positron angle is measured with respect to the positive  $Z$  direction.

The ISR sample is selected by requiring that a photon with energy  $E_\gamma$  be detected in the LUMI photon calorimeter. The variables  $Q^2$  and  $x$  are determined using equations 5 and 6 replacing  $E_e$  with  $E_e - E_\gamma$ , treating the virtual positron as a real positron, which is a good approximation for the ISR analysis.

### 4.1 Vertex determination

The vertex coordinates are determined from tracks reconstructed with the CTD and VXD. The  $Z$  coordinate is determined on an event-by-event basis. Since the transverse sizes of the beams are smaller than the resolutions for the  $X$  and  $Y$  coordinates of the vertex, the beam positions averaged over the entire data sets are used. For events which do not have a tracking vertex, the  $Z$  coordinate is set to the

primary position of the interaction point. For events with a tracking vertex, the resolution of  $Z$  is  $\pm 0.4 \text{ cm}$  over the entire  $Z$  range considered in these analyses. At low  $y$  the current jet is produced at small forward angles, resulting in a reduced probability for vertex reconstruction. The vertex distributions for the two analyses, including events arising from the interaction of the satellite bunch, are found to be well reproduced by the MC simulation.

### 4.2 Positron identification and efficiency

The positron identification algorithm is based on a neural network using information from the CAL and is described elsewhere [26]. The efficiency of finding the scattered positron is sensitive to details of the shower evolution, in particular to energy loss in material between the interaction point and the calorimeter. The efficiency was measured using elastic QED Compton events  $ep \rightarrow e\gamma p$  where the positron and photon are detected in the CAL by exploiting the presence of two electromagnetic objects and the over-constrained kinematics. DIS data were also used to study the positron finding efficiency by comparing different positron finding algorithms. A correction based on the QED Compton study is used in the analyses. The size of the correction to the efficiency obtained from the standard ZEUS detector simulation programme is 16% at 8 GeV decreasing to 0% at 18 GeV. The efficiency of the identification algorithm when the scattered positron has an energy of 10 GeV is 55%, rising to 100% above energies of 18 GeV. The uncertainty in the efficiency is accounted for in the systematic errors (see Sect. 5.5).

### 4.3 Positron position measurement

The impact point of the scattered positron at the calorimeter is measured using the SRTD for the SVX data and part of the ISR data. The position resolution of the SRTD is determined using positrons hitting the calorimeter at the boundary of cells where the position can be determined by the calorimeter with a resolution of less than 0.1 cm. The measured SRTD position resolution of 0.3 cm is well reproduced by the MC simulation.

For events with a reconstructed vertex the scattering angle of the positron, determined from the event vertex and the impact position at the face of the SRTD, has a resolution of 1.7 mrad, while for events without a tracking vertex the measured scattering angle has a resolution of 4 mrad. For the ISR analysis, 7% of the events are found outside the SRTD. For these events, the impact point is determined by the RCAL resulting in an angular resolution of 7 mrad.

### 4.4 Positron energy measurement

In the analyses,  $x$  and  $Q^2$  are determined using the corrected positron energy  $E'_e$  as described below. For background rejection and rejection of events with hard initial state radiation, we define, in addition, the quantity  $\delta$ :



$$\delta = \delta_h + \delta_e; \quad \delta_h = \sum_h E_h (1 - \cos \theta_h); \quad \delta_e = E'_e (1 - \cos \theta_e), \quad (7)$$

where  $E_h$  is the energy deposited in the calorimeter cell  $h$  and the angle,  $\theta_h$ , is determined from the event vertex and the cell centre. The sum excludes the calorimeter cells belonging to the scattered positron.  $\delta_e$  is calculated using the corrected positron energy.

In the  $Q^2$  range of the present analyses the scattered positron traverses typically two radiation lengths of passive material before reaching the calorimeter, thereby losing a significant amount of energy. The correlation between the energy lost in the inactive material in front of the calorimeter and the energy deposited in the SRTD is used to correct the calorimeter energy measurement.

This correction can be determined from a data sample where the scattered positron energy is known from kinematic constraints. This is the case for DIS events with  $x = E_e/E_p$ , for which the scattered positron energy is equal to the incident positron beam energy. Events close to this condition, called kinematic peak (KP) events, can be selected by the requirement  $\delta_h < 0.06 \cdot E_e$ . The correction for lower energies can be obtained using QED Compton events. The energies of the positron and the photon can be predicted precisely from the measurement of their scattering angles assuming the transverse momentum of the scattered proton to be small. Events from elastic DIS  $\rho^0$  production,  $ep \rightarrow epp^0$ ;  $\rho^0 \rightarrow \pi^+\pi^-$ , provide a way to check the SRTD energy correction. Here, the angle of the positron is determined from the event vertex and the position measurement at the face of the SRTD while the momenta of the  $\pi^+$  and  $\pi^-$  are measured with the CTD.

The SRTD energy correction is determined using the KP and QED Compton events. A clear correlation between the energy measured in the calorimeter and the energy deposited in the SRTD for KP events is observed (see Fig. 1a). Figure 1b compares the corrected positron energies of the data with the MC simulation for KP events, where it can be seen that the peak and width of the data are well reproduced by the MC simulation. The deviation of the mean corrected energy from the prediction of the KP and QED Compton events is less than 2% as shown in Fig. 1c for positron energies between 9 and 27.5 GeV. The point at the highest energy ( $E'_e = 27.5$  GeV) is obtained from the KP events while the lower energy points are determined from the elastic QED Compton events. For the DIS  $\rho^0$  data, the deviation of the mean corrected positron energy from the value expected from the  $\rho^0 \rightarrow \pi^+\pi^-$  measurement is less than 1% (see Fig. 1c); these data have not been used to determine the SRTD energy correction. The resolution of the corrected positron energy is shown in Fig. 1d and can be described by  $\sigma/E = 26\%/\sqrt{E(\text{GeV})}$ .

## 5 Analysis of the shifted vertex data

In the SVX analysis,  $F_2$  is measured using data from an integrated luminosity of  $58 \text{ nb}^{-1}$  collected with the vertex shifted by +67 cm in  $Z$ . The vertex shift extends the acceptance of positrons to smaller scattering angles and hence events with lower  $Q^2$  can be reconstructed.

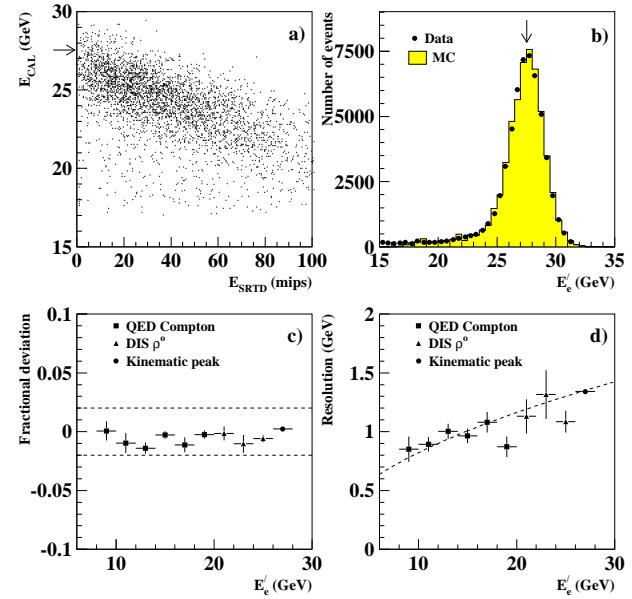


**Fig. 1.** **a)** The correlation between the energy measured in the calorimeter and the energy in the SRTD in units of mips (mean energy deposited by one minimum ionising particle) for the kinematic peak (KP) events. **b)** The distribution of the corrected positron energy for the data, shown as the points, and the MC simulation, shown as the histogram, for KP events. The arrows in **a)** and **b)** indicate the positron beam energy. **c)** Measured fractional deviation between the mean corrected calorimeter energy and the predicted energy as a function of the corrected energy. **d)** The measured energy resolution of the calorimeter as a function of energy. The curve corresponds to  $26\% \cdot \sqrt{E(\text{GeV})}$ , the resolution used in the MC simulation. For **c)** and **d)**, the data are results using QED Compton (squares), DIS elastic  $\rho^0$  (triangles) and KP (dots) events. See text for details

### 5.1 Event selection

The following cuts are used to select the DIS events for the SVX analysis.

- The scattered positron energy as obtained from the calorimeter and corrected by the energy measured in the SRTD is required to be greater than 10 GeV. This ensures a high efficiency of finding the scattered positron and removes high  $y$  events which suffer from large photoproduction background.
- The impact position of the scattered positron is required to be at least 3 cm from the inner edge of the rear calorimeter. This cut ensures that the electromagnetic shower of the positron is well contained in the calorimeter. The impact position of the scattered positron is required to be within the acceptance of the SRTD and at least 1 cm away from the edges of the SRTD.
- The value of  $\delta$  for the event is required to be within  $35 < \delta < 65$  GeV in order to reduce photoproduction and beam-gas related background. This requirement also removes events with hard initial state radiation, thus reducing the radiative corrections. The hadronic energy measurement affects the event selection via this cut when  $\delta_e < 35$  GeV. The simulation of  $\delta_h$  in the MC is sensitive to the hadronisation scheme and the details of the hadronic energy loss in the inactive material. The mean  $\delta_h$  was compared to  $\delta_e$  as a function of  $\delta_e$  and the MC simulation was found to reproduce the data adequately.

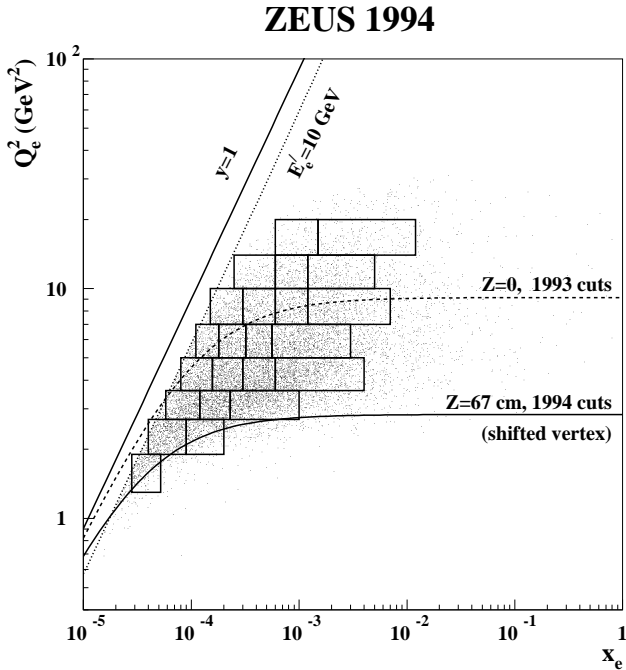


**Fig. 2.** The  $x$ - $Q^2$  distribution for events passing the selection criteria from the 1994 SVX analysis. The extension in the accepted region compared to the 1993 analyses is shown between the dashed line labeled “ $Z=0$ , 1993 cuts” and the solid line labeled “ $Z=67$  cm, 1994 cuts (shifted vertex)”. See text for more details

- For events with a tracking vertex, the  $Z$  coordinate of the vertex is required to be within  $25 \text{ cm} < Z < 200 \text{ cm}$ , the acceptance being extended to larger  $Z$  values to accommodate the events from the satellite bunch. If no vertex was reconstructed, the  $Z$  coordinate is set to the primary interaction point.

A total of 13210 events pass the selection cuts.

The distributions of the reconstructed  $x$  and  $Q^2$  for the selected events are shown in Fig. 2. The dashed line ( $Z=0$ , 1993 cuts) gives the limit of the acceptance for the scattered positron corresponding to the 1993  $F_2$  measurement using the ZEUS detector. The acceptance limit in this analysis is shown as the solid line ( $Z=67$  cm, 1994 cuts). The region between the dashed and solid lines shows the increased acceptance obtained for the SVX data and by using the SRTD.

### 5.2 Resolution of the kinematic variables and bin selection

The selected events are binned as shown in Fig. 2. The sizes of the bins are determined by the resolution in  $x$  and  $Q^2$ . Within the selected bins, the resolution in  $Q^2$  is found to be 9-12% and the systematic shifts are less than 5% as determined from MC simulation. At the lowest values of  $x$ , the resolution in  $x$  is 20% increasing to 85% for larger  $x$  values where larger bins are chosen to ensure a high purity (defined as the number of events measured in the bin which originated from the bin divided by the number of events measured in the bin). The average reconstructed values of  $x$  are typically shifted by 6%, with shifts of up to 28% occurring at the lowest  $y$  values. The bias in the bins results from the steepness of the distribution and the radiative events.

The purity of the events in the bins is typically about 45% and is greater than 30% for all bins. The acceptance (defined as the number of measured events originating from the bin divided by the number of events generated in the bin) is typically 70% except for the lowest  $Q^2$  bin where it is about 22%, and for the bin with  $1.9 \text{ GeV}^2 < Q^2 < 2.7 \text{ GeV}^2$  and  $0.9 \times 10^{-4} < x < 2.0 \times 10^{-4}$  where it is 27%. In these bins the purity is 50% and 36% respectively.

### 5.3 Background estimation

The background from beam-gas related interactions is estimated from events due to the unpaired bunches of positrons and protons. Events triggered from empty bunch crossings are used to estimate the background from cosmic ray showers. The surviving background events are subtracted statistically. The  $(x, Q^2)$  bin with the highest background has 2% background. In the other bins no events survive and the background is estimated to be less than 1%.

The largest contributor to background is photoproduction, where an energy deposit in the calorimeter is misidentified as a scattered positron. This background is estimated in two ways. The first method uses the photoproduction MC simulation. The same selection procedure as for DIS events is applied and the accepted photoproduction events are statistically subtracted for each  $(x, Q^2)$  bin. The second method uses the  $\delta$  distribution to estimate the background. The two estimates are found to agree within statistical errors. The photoproduction background is found to be significant only in bins corresponding to the highest  $y$  values where it amounts to 2%.

### 5.4 Determination of $F_2$

In the  $Q^2$  range of the present analysis, the effect from  $Z^0$  exchange is negligible and the double differential cross section for single virtual photon exchange in DIS is given by

$$\frac{d^2\sigma}{dx dQ^2} = \frac{2\pi\alpha^2}{xQ^4} \left[ 2(1-y) + \frac{y^2}{1+R} \right] \times F_2(x, Q^2) [1 + \delta_r(x, Q^2)], \quad (8)$$

where  $R$  is related to the longitudinal structure function,  $F_L$ , by  $R = F_L/(F_2 - F_L)$ . The correction to the Born cross section from radiative effects is given by  $\delta_r$ . In the analysis, hard radiation collinear with the final state positron is not resolved. Furthermore, the event selection criteria (see above) remove events with hard radiation collinear with the beam positron. Thus, in the kinematic range covered in this analysis, the effective radiative correction is typically 10% or less and is, to a sufficient approximation, independent of the structure function  $F_2$ .

An iterative procedure is used to extract the structure function  $F_2$ . In the first step a bin-by-bin correction obtained from the MC simulation using the parton distributions given by MRSA[22, 23] is applied to the data. The result for  $F_2$  from this first iteration is used for a QCD fit using DGLAP equations [27] in next-to-leading order (QCD NLO fit) very similar to that described in [5]. The evolution uses massless

## ZEUS 1994

quarks of three flavours in the proton, and the charm quark coefficient functions from [28] to ensure a smooth crossing of the charm threshold; the charm contribution to  $F_2$  is calculated in leading order only. The NMC [29] data for  $Q^2 > 4 \text{ GeV}^2$  are used to constrain the fit at high  $x$ . The value of  $R$  was taken using the QCD prescription [30] and the parton distributions from the QCD NLO fit. The effect of the  $R$  correction on the  $F_2$  values is significant only in the highest  $y$  bins where it is as much as 7%.

The resulting QCD NLO fit parameters are used to reweight the MC events, and the procedure is repeated, leading to a new estimate of  $F_2$ . The procedure is repeated until the  $F_2$  values from two consecutive iterations change by less than 0.5%. The final result is reached in three iterations. It should be noted that the QCD NLO fit is used here only as a parameterisation to obtain a stable acceptance correction and not to perform a QCD analysis.

The statistical errors of the  $F_2$  values are calculated from the number of events measured in the bins and the statistical error on the acceptance calculation from the MC simulation. Since we are using bin-by-bin corrections, the correlations of statistical errors between the  $F_2$  measurements enter only via the finite statistics of the MC sample. The correlations are small given the relatively large MC sample used in this analysis. A correlation between the  $F_2$  values of neighbouring bins is present due to the acceptance and smearing corrections. The sensitivity of the measured  $F_2$  to this effect has been checked by using the  $F_2$  obtained from the MRSA [22] parton density parameterisations, modified at low  $Q^2$  as described in [23], for the acceptance correction calculations. The change in the measured  $F_2$  values is found to be small compared to the statistical errors.

The measured distributions of  $Q^2$  and  $x$  are shown in Figs. 3a and 3b respectively. The data are shown as the solid circles and the MC simulation results, normalised to the luminosity of the data and reweighted by the QCD NLO fit, are shown as histograms. The measured distributions of the positron energy and angle are shown in Figs. 3c and 3d. All events which pass the selection criteria described in Sect. 5.1 with a reconstructed  $Q^2 > 1 \text{ GeV}^2$  are shown, including those events which fall outside the bins used for the analysis. These distributions have not been corrected for background. There is adequate agreement between data and simulation for both the shape and normalisation of the distributions. The number of events, and values of  $R$  and  $F_2$  at  $x$  and  $Q^2$  values specified, which are chosen to be convenient for comparisons with other  $F_2$  measurements, are given in Table 1. The functional form of the QCD NLO fit was used to calculate  $F_2$  at these  $x$  and  $Q^2$  values. Using alternate parameterisations for this correction has a negligible effect on the quoted values of  $F_2$ .

### 5.5 Systematic uncertainties

The systematic uncertainty of the  $F_2$  values is determined by changing the selection cut or analysis procedure and taking the difference between the measured value of  $F_2$  and the new value. Positive and negative differences are separately added in quadrature to obtain the total systematic error. For each

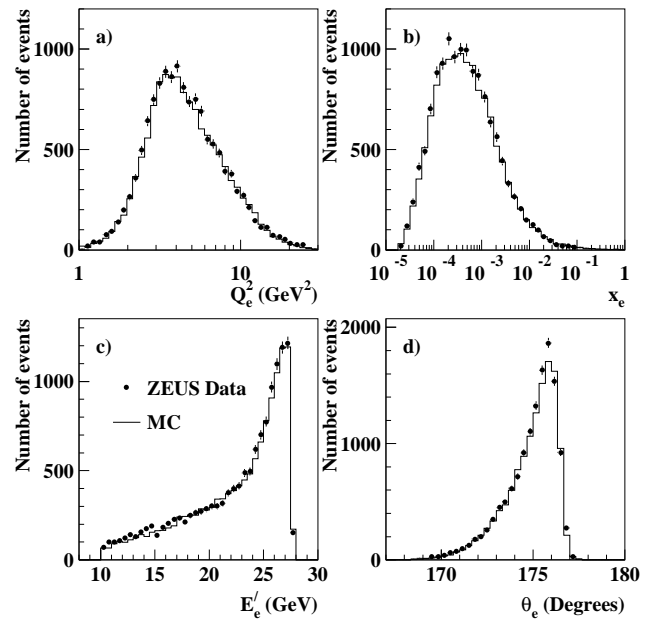


**Fig. 3.** **a)** The reconstructed  $Q_e^2$  of the SVX event sample. **b)** The reconstructed  $x_e$  distribution of the SVX event sample. **c)** The spectrum of the scattered positron energy. **d)** The distribution of the positron scattering angles. In the figures the data (dots) are compared with the MC simulation (histograms). All events with a reconstructed  $Q_e^2 > 1 \text{ GeV}^2$  which pass the selection criteria described in Sect. 5.1 are shown. The background has not been subtracted from the data. The MC distributions have been reweighted using the final  $F_2$  parameterisation from the QCD NLO fit to the ZEUS data and normalised to the luminosity of the data

change, the photoproduction background estimated from the MC simulation is first subtracted.

The systematic uncertainties are grouped in the following categories:

#### Positron energy and finding efficiency

- The parameters of the neural network positron finder are varied resulting in changes of  $F_2$  by typically less than 4%. In addition, an alternate positron finder, which has been used in previous analyses [1], is used as a check of the neural network finder. Consistent results are obtained in the region where the efficiencies of both finders are reasonably high.
- In the MC simulation the reconstructed positron energy is increased and decreased by a linear function (2% at 5 GeV and 1% at 27.5 GeV). The magnitude of the shift represents our present understanding of the energy scale. These shifts have a 5% effect on  $F_2$  for the low  $x$  bins and 10% for the highest  $x$  bins.
- The positron identification efficiency is varied within the errors of its determination based on the QED Compton study. The effect on  $F_2$  is negligible except in the lowest  $x$  bins where it is as much as 3%. This also checks the effects of a possible energy dependence of the trigger efficiency.

**Table 1.** The measured  $F_2(x, Q^2)$  from the SVX analysis. The bin boundaries and values of  $x$  and  $Q^2$  at which  $F_2$  is determined are listed. The numbers of events before background subtraction as well as the estimated photoproduction and beam-related background (in the column labeled “No. BG events”) for each bin are given. The values of  $R$ , which are used to determine  $F_2$  from the differential cross sections, are shown (see text). An overall normalisation error of 3% is not included. Note that the systematic errors between different bins are correlated

$Q^2$ GeV <sup>2</sup>	$Q^2$ range GeV <sup>2</sup>	$x$	$x$ range	No. events	No. BG events	$R$	Measured $F_2 \pm \text{stat} \pm \text{sys}$
1.5	1.3 - 1.9	$3.5 \cdot 10^{-5}$	$2.8 - 5.2 \cdot 10^{-5}$	292	14.6	0.71	$0.79 \pm 0.06 \pm_{0.11}^{0.07}$
2.0	1.9 - 2.7	$6.5 \cdot 10^{-5}$	$4.0 - 9.0 \cdot 10^{-5}$	747	20.0	0.59	$0.93 \pm 0.04 \pm_{0.08}^{0.06}$
3.0	2.7 - 3.6	$1.2 \cdot 10^{-4}$	$0.9 - 2.0 \cdot 10^{-4}$	456	2.7	0.53	$0.71 \pm 0.04 \pm_{0.05}^{0.06}$
		$6.5 \cdot 10^{-5}$	$0.58 - 1.2 \cdot 10^{-4}$	600	17.3	0.57	$1.13 \pm 0.06 \pm_{0.09}^{0.06}$
4.5	3.6 - 5	$2.0 \cdot 10^{-4}$	$1.2 - 2.3 \cdot 10^{-4}$	706	1.3	0.49	$0.95 \pm 0.04 \pm_{0.07}^{0.08}$
		$4.5 \cdot 10^{-4}$	$0.23 - 1.0 \cdot 10^{-3}$	1067	0	0.44	$0.74 \pm 0.03 \pm_{0.06}^{0.10}$
		$1.2 \cdot 10^{-4}$	$0.8 - 1.57 \cdot 10^{-4}$	503	12.0	0.52	$1.12 \pm 0.06 \pm_{0.08}^{0.07}$
6.0	5 - 7	$2.0 \cdot 10^{-4}$	$1.57 - 3.0 \cdot 10^{-4}$	643	1.3	0.50	$1.10 \pm 0.05 \pm_{0.04}^{0.08}$
		$4.5 \cdot 10^{-4}$	$3.0 - 6.0 \cdot 10^{-4}$	705	0	0.45	$0.93 \pm 0.04 \pm_{0.09}^{0.10}$
		$1.2 \cdot 10^{-3}$	$0.6 - 4.0 \cdot 10^{-3}$	1148	0	0.39	$0.72 \pm 0.03 \pm_{0.05}^{0.10}$
		$1.2 \cdot 10^{-4}$	$1.1 - 1.8 \cdot 10^{-4}$	289	8.0	0.53	$1.58 \pm 0.10 \pm_{0.13}^{0.11}$
8.5	7 - 10	$2.0 \cdot 10^{-4}$	$1.8 - 3.2 \cdot 10^{-4}$	389	1.3	0.50	$1.08 \pm 0.06 \pm_{0.05}^{0.07}$
		$4.5 \cdot 10^{-4}$	$3.2 - 5.6 \cdot 10^{-4}$	410	0	0.46	$0.98 \pm 0.06 \pm_{0.05}^{0.09}$
		$1.2 \cdot 10^{-3}$	$0.56 - 3.0 \cdot 10^{-3}$	1016	0	0.40	$0.78 \pm 0.03 \pm_{0.09}^{0.09}$
		$2.0 \cdot 10^{-4}$	$1.5 - 3.0 \cdot 10^{-4}$	268	4.0	0.51	$1.57 \pm 0.11 \pm_{0.08}^{0.13}$
		$4.5 \cdot 10^{-4}$	$3.0 - 6.0 \cdot 10^{-4}$	314	1.3	0.47	$0.99 \pm 0.06 \pm_{0.06}^{0.10}$
12.0	10 - 14	$8.0 \cdot 10^{-4}$	$0.6 - 1.2 \cdot 10^{-3}$	333	0	0.44	$0.93 \pm 0.06 \pm_{0.08}^{0.10}$
		$2.6 \cdot 10^{-3}$	$1.2 - 7.0 \cdot 10^{-3}$	542	0	0.36	$0.66 \pm 0.03 \pm_{0.06}^{0.08}$
		$4.5 \cdot 10^{-4}$	$2.5 - 6.0 \cdot 10^{-4}$	124	2.7	0.48	$0.99 \pm 0.09 \pm_{0.08}^{0.03}$
15.0	14 - 20	$8.0 \cdot 10^{-4}$	$0.6 - 1.2 \cdot 10^{-3}$	167	0	0.45	$0.98 \pm 0.08 \pm_{0.07}^{0.07}$
		$2.6 \cdot 10^{-3}$	$1.2 - 5.0 \cdot 10^{-3}$	291	0	0.37	$0.73 \pm 0.05 \pm_{0.08}^{0.06}$
		$8.0 \cdot 10^{-4}$	$0.6 - 1.5 \cdot 10^{-3}$	81	0	0.46	$1.33 \pm 0.16 \pm_{0.06}^{0.10}$
		$2.6 \cdot 10^{-3}$	$0.15 - 1.2 \cdot 10^{-2}$	171	0	0.38	$0.91 \pm 0.07 \pm_{0.11}^{0.04}$

### Positron scattering angle

- Changing the fiducial cut of the positron position at the inner edge of the calorimeter from 3 cm to 4 cm has a 3% effect on  $F_2$  for the lowest  $x$  and  $Q^2$  bins.
- The reconstructed  $Z$  vertex position in the MC simulation is shifted by  $\pm 0.4$  cm in  $Z$ . The effect on  $F_2$  is less than 1.5% for all the bins.
- The positron position reconstructed by the SRTD is shifted by  $\pm 0.2$  cm in  $X$  and  $\pm 0.15$  cm in  $Y$ . The size of the shifts are estimated from the uncertainty of the position of the SRTD relative to the beam position in  $X$  and  $Y$ . These shifts have a 7% effect on  $F_2$  for the lowest  $x$  bins and less than 4% for the other bins.

### Additional systematic uncertainties

- The photoproduction background estimate is changed by +100% and –50% resulting in a 2% effect on  $F_2$  for the lowest  $x$  bins and a negligible effect for the higher  $x$  bins.
- In the calculation of the acceptance, the fraction of the total cross section arising from diffractive scattering is increased by 60%. The effect on  $F_2$  is less than 5%.
- The efficiency for reconstructing a vertex is determined by MC simulation and is found to decrease from 85% at  $y = 0.7$  to 40% at  $y = 0.03$ . For events at low  $y$  the tracks in the CTD are at low angles as the current jet is produced in the forward direction, resulting in a reduced probability of reconstructing the event vertex. In the data, 70% of the events have a tracking vertex compared to 73% in the MC simulation. The vertex of the events

without a tracking vertex is set to the nominal shifted vertex position. The reconstructed  $Q^2$  values are larger than the true  $Q^2$  values if the events without a tracking vertex originated from the satellite bunch. The effect on  $F_2$  of the satellite bunch was studied by MC simulation and it was found to be largest at high  $x$  values where it is 8% decreasing to about 1% for the low  $x$  points.

As an additional check, the  $Z$  coordinate of the vertex is fixed at the primary interaction point for all events in the data and in the MC simulation in order to check the sensitivity to the vertex distribution. The change in  $F_2$  is largest for the high  $Q^2$  values at large  $x$  where it is about 15% of  $F_2$ . For the lowest  $x$  and  $Q^2$  bins the effect on  $F_2$  is about 10%, while for the other bins it is less than 5%. The change in  $F_2$  from this systematic check is not included when determining the systematic error.

- The  $\delta$  cut is lowered from 35 GeV to 32 GeV and raised to 38 GeV. The largest effect on  $F_2$  of about 3% occurs at the low  $x$  and low  $Q^2$  bins, and it decreases with increasing  $Q^2$  and  $x$ . Changing the  $\delta$  cut checks the photoproduction background estimate, the simulation of the QED radiative effects and the simulation of the hadronic energy measurement.

The total systematic error on  $F_2$  of this analysis is 4 to 14% to be compared with the statistical error of 4 to 9%, which includes the statistical error from the MC simulation (see Table 1). In addition to the above errors, there is an overall normalisation uncertainty of 3% due to the uncertainty in the first level trigger efficiency and to the uncertainty on the determination of the luminosity. The given errors of the  $F_2$  data do not include this normalisation uncertainty.

## 6 Analysis of the radiative events

The ISR analysis is based on data, corresponding to an integrated luminosity of  $2.5 \text{ pb}^{-1}$ , taken in 1994 with the interaction point at  $Z = 0$ .  $F_2$  is measured using events with QED initial state radiation. The emission of a hard photon from the initial state positron results in a scattering at a reduced centre-of-mass energy, and thus for a given scattering angle events with lower  $Q^2$  are accepted.

### 6.1 Event selection and bin selection

The sample of DIS events with initial state radiation is selected in a manner identical to the SVX analysis, with the following exceptions:

- An energy deposit in the LUMI photon calorimeter is demanded to ensure collinear radiation. The energy is required to be between 6 and 18 GeV in order to reduce background and ensure sufficient resolution of the reconstructed kinematic variables. Events having an energy greater than 3 GeV measured in the electron calorimeter of the luminosity detector are rejected in order to reduce the accidental overlap of DIS and photoproduction with those from the bremsstrahlung process  $ep \rightarrow e\gamma p$ .
- The corrected energy of the scattered positron detected in the RCAL is required to be greater than 8 GeV. For positrons within the fiducial volume of the SRTD, the energy is corrected as in the SVX analysis. In areas not covered by the SRTD a position dependent description of the inactive material in front of the CAL is determined using the KP events and is used to correct the measured energy in the CAL. A description of the method can be found in [1]. A correction for the positron identification efficiency in the MC simulation is also made as in the SVX analysis.
- The fiducial cut for the positron position is the same as that described in the SVX analysis for the inner edge of the SRTD. If the positron position is outside the fiducial volume of the SRTD, the position is reconstructed using the calorimeter.
- The  $\delta$  cut is replaced by a cut on  $\delta' = \delta + 2 \cdot E_\gamma$ .

A sample of 10726 events is selected. The resolutions of  $x$  and  $Q^2$  are similar to those given in Sect. 5.2 and depend only weakly on the photon energy  $E_\gamma$ . The bins in  $x$  and  $Q^2$  are chosen in a similar way to those used in the SVX analysis.

### 6.2 Background estimation

The main source of background is the accidental overlap of DIS or photoproduction events with bremsstrahlung events,  $ep \rightarrow e\gamma p$ . This background is estimated with events selected with the above criteria, removing the requirement of a tagged photon and the  $\delta'$  cut. To these events a photon is added with an energy determined from a random sampling of the measured spectrum of photon energies for bremsstrahlung events. The resulting  $\delta'$  spectrum is normalised to the  $\delta'$  distribution of the data above 70 GeV

## ZEUS 1994

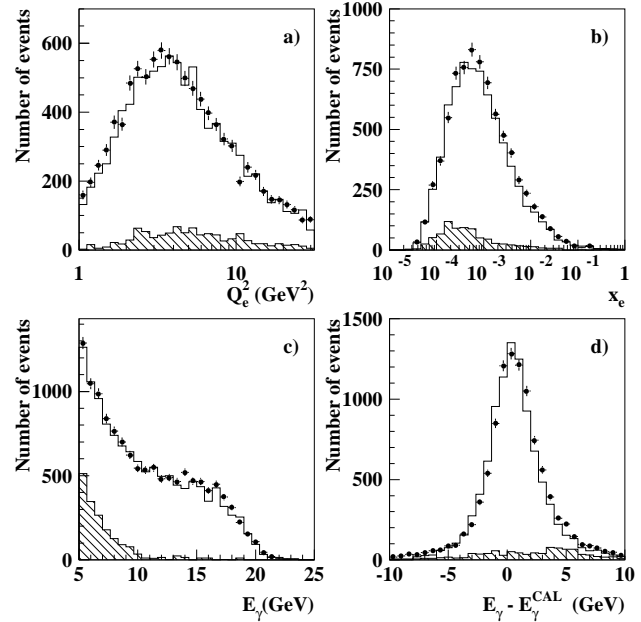


**Fig. 4.** a) The reconstructed  $Q_e^2$  distribution of the ISR sample. b) The reconstructed  $x_e$  distribution of the ISR sample. c) The spectrum of the photon energy measured in the LUMI photon calorimeter without the cut on the photon energy. d) The difference between the photon energy measured in the LUMI photon calorimeter and that determined from the CAL. In the figures the data (dots), background estimate (hatched histogram) and sum of the background and DIS MC (solid histogram) are shown. All events with a reconstructed  $Q_e^2 > 1 \text{ GeV}^2$  which pass the selection criteria described in Sect. 6.1 are shown. The MC distributions have been reweighted using the final  $F_2$  parameterisation from the QCD NLO fit to the ZEUS data and normalised to the luminosity of the data

where no DIS events are possible, taking energy and momentum conservation and the resolution of the detector into consideration, to obtain an estimate of the background. It is subtracted from the data for each  $(x, Q^2)$  bin and is below 10% of the number of events observed in the bin except in the lowest  $x$  bins where it is up to 24% in one bin.

The beam related background is determined and subtracted statistically in the same manner as described in Sect. 5.3. It is below 5% for the three lowest  $Q^2$  bins except for the bin at the lowest  $x$  where it is 7%. It is negligible in higher  $Q^2$  bins. The background from photoproduction with initial state radiation and cosmic rays is negligible. Event losses due to bremsstrahlung overlap with a DIS event having initial state radiation are also negligible.

### 6.3 Determination of $F_2$

$F_2$  is determined as described in Sect. 5.4. The MC sample is first reweighted using the QCD NLO fit to the  $F_2$  from the SVX analysis.  $F_2$  is then determined using the reweighted MC for the acceptance correction. A second QCD NLO fit to the measured ISR  $F_2$  values (excluding the SVX  $F_2$  values) is performed and the final  $F_2$  is determined. The measured distributions of  $Q^2$  and  $x$  are shown in Figs. 4a and 4b respectively. The data are seen to be in adequate agreement with the MC simulation after the background is added.

The photon energy spectrum of the selected events without the cut on  $E_\gamma$  is shown in Fig. 4c and is well described by the expectation from the DIS MC simulation and background estimates. Figure 4d shows the difference between the energy of the radiated photon measured in the LUMI photon calorimeter and  $E_\gamma^{CAL}$ , the photon energy determined, using energy and momentum conservation, from the measurements of the energies and the angles of the scattered positron and hadrons in the CAL. The agreement between the MC simulation and the data is reasonable. The distribution is centred at zero indicating agreement in the energy scales of the LUMI photon calorimeter and the CAL.

#### 6.4 Systematic uncertainties

The checks used to estimate the systematic uncertainty are similar to those presented in Sect. 5.5 except for the checks related to the displacement of the vertex. To estimate the uncertainties due to the photon tagging the following additional checks are made:

- The lower cut on the photon energy is raised from 6 to 7 GeV. The effect on  $F_2$  is below 2.5% for the bins at low  $y$  and around 6% for the bins at high  $y$  and is compatible with statistical fluctuations.
- The resolution of the photon energy measurement in the MC simulation is degraded from  $26.5\% \cdot \sqrt{E}(\text{GeV})$  to  $28.5\% \cdot \sqrt{E}(\text{GeV})$ . The effect on  $F_2$  is around 1.5%.
- The energy calibration of the LUMI photon calorimeter in the MC simulation is changed linearly, within the estimated uncertainties, by 0.4% at the positron beam energy to 3% at 5 GeV. The effect on  $F_2$  is around 7%.
- The acceptance of the LUMI photon calorimeter for ISR events obtained from the MC simulation is about 30%. An independent determination of the acceptance using bremsstrahlung data leads to an effect of about 4% on  $F_2$ .
- The beam divergence is determined with the LUMI photon calorimeter using the bremsstrahlung events. If the beam divergence is increased by 15% in the acceptance calculation, the effect on  $F_2$  is, on average, 1.7%.
- The event selection is repeated without the requirement that the LUMI electron energy be less than 3 GeV. The effect is below 3% for the bins at low  $y$  and is up to 10% in two bins at high  $y$ .

The total systematic uncertainty of this analysis is 14 to 27% to be compared to the statistical error of 7 to 14%. The effect of additional QED radiative corrections not included in the HERACLES MC programme is small relative to the measurement errors in the kinematic region considered here [31].

## 7 Results and discussion

The measured  $F_2$  values from the SVX data (ZEUS SVX 1994) are listed in Table 1, and those from the ISR analysis (ZEUS ISR 1994) are listed in Table 2. The data are

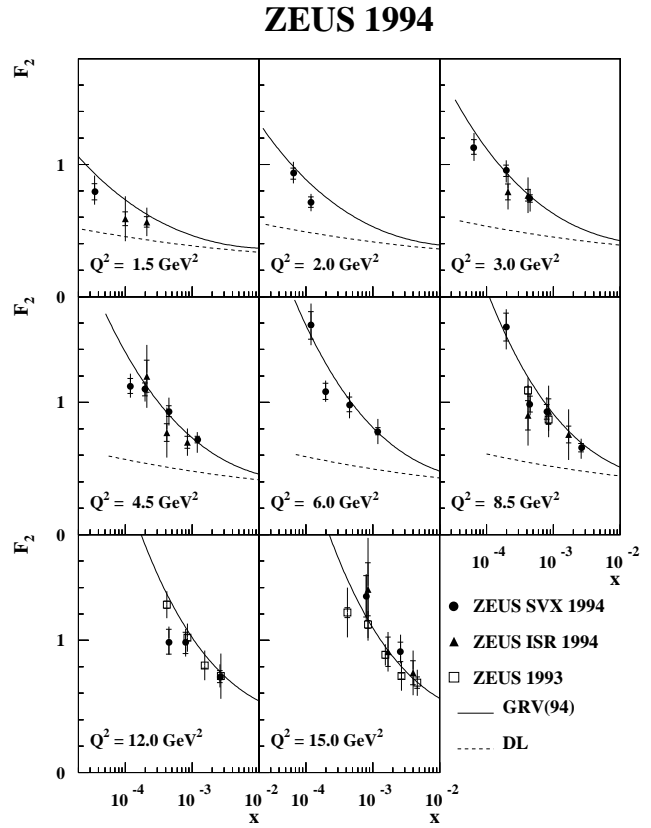


**Fig. 5.** The measured  $F_2$  from the SVX analysis (solid dots), the ISR analysis (solid triangles) and the 1993 results (open squares) compared with the expectations from GRV(94) (solid line) and Donnachie and Landshoff (DL) (dashed line). Overall normalisation uncertainties of 3% for the 1994 results and 3.5% for the 1993 points are not shown. The inner error bars represent the statistical errors while the outer error bars represent the systematic errors added in quadrature to the statistical errors

presented in Fig. 5 together with previous ZEUS measurements (ZEUS 1993). The three data sets are in good agreement. The present analyses significantly increase the measured kinematic region. Using our data alone, the rise of  $F_2$  as  $x$  decreases is observed down to  $Q^2 = 3 \text{ GeV}^2$ . Including the fixed target data (the  $F_2$  parameterisations shown as curves in Fig. 5 provide a good description of the fixed target data at higher  $x$ ) the rise is seen to persist down to  $Q^2 = 1.5 \text{ GeV}^2$ .

In Fig. 5 the measured  $F_2$  values are compared to the prediction of GRV(94) [32] which is based on perturbative QCD using the DGLAP evolution equations. The GRV(94) parton distributions have a very low starting scale,  $Q_0^2$ , for the DGLAP evolution equation of  $0.34 \text{ GeV}^2$ , where the gluon and sea distributions are assumed to have valence-like spectra. The steep rise in  $F_2$  at low  $x$  is generated dynamically by the evolution in  $Q^2$ . The GRV(94) predictions for  $F_2$  are in agreement with the data showing that perturbative QCD can describe the data down to  $Q^2$  values of  $1.5 \text{ GeV}^2$  at the low  $x$  values of this measurement. The predictions of Donnachie and Landshoff [33] based on Regge phenomenology are also shown and are seen to be ruled out for  $Q^2 \geq 2 \text{ GeV}^2$  and disfavoured for  $Q^2 = 1.5 \text{ GeV}^2$ .

**Table 2.** The measured  $F_2(x, Q^2)$  from the ISR analysis. The bin boundaries and values of  $x$  and  $Q^2$  at which  $F_2$  is determined are listed. The numbers of events before background subtraction as well as the estimated accidental event overlap and beam-related background (in the column labeled “No. BG events”) for each bin are given. The value of  $R$  obtained from the NLO QCD fit is tabulated. An overall normalisation error of 3% is not included. Note that the systematic errors between different bins are correlated

$Q^2$ GeV <sup>2</sup>	$Q^2$ range GeV <sup>2</sup>	$x$	$x$ range	No. events	No. BG events	$R$	Measured $F_2 \pm \text{stat} \pm \text{sys}$
1.5	1.3 - 2.2	$1.0 \cdot 10^{-4}$	$0.65 - 1.5 \cdot 10^{-4}$	273	34.4	0.72	$0.59 \pm 0.05 \pm 0.16$
		$2.1 \cdot 10^{-4}$	$1.5 - 4.5 \cdot 10^{-4}$	474	16.5	0.61	$0.57 \pm 0.04 \pm 0.10$
3.0	2.2 - 3.8	$2.1 \cdot 10^{-4}$	$1.5 - 3.0 \cdot 10^{-4}$	429	68.5	0.57	$0.79 \pm 0.06 \pm 0.12$
		$4.2 \cdot 10^{-4}$	$3.0 - 9.0 \cdot 10^{-4}$	695	49.5	0.52	$0.77 \pm 0.05 \pm 0.13$
4.5	3.8 - 6.5	$2.1 \cdot 10^{-4}$	$1.5 - 3.0 \cdot 10^{-4}$	265	55.7	0.56	$1.20 \pm 0.12 \pm 0.21$
		$4.2 \cdot 10^{-4}$	$3.0 - 6.0 \cdot 10^{-4}$	340	59.8	0.51	$0.77 \pm 0.07 \pm 0.18$
		$8.5 \cdot 10^{-4}$	$0.6 - 1.8 \cdot 10^{-3}$	570	42.5	0.47	$0.70 \pm 0.05 \pm 0.09$
8.5	6.5 - 11.5	$4.2 \cdot 10^{-4}$	$3.0 - 6.0 \cdot 10^{-4}$	189	45.6	0.52	$0.90 \pm 0.11 \pm 0.20$
		$8.5 \cdot 10^{-4}$	$0.6 - 1.2 \cdot 10^{-3}$	246	31.2	0.48	$0.93 \pm 0.10 \pm 0.17$
		$1.7 \cdot 10^{-3}$	$1.2 - 3.6 \cdot 10^{-3}$	341	15.0	0.43	$0.76 \pm 0.06 \pm 0.18$
15.0	11.5 - 20	$8.5 \cdot 10^{-4}$	$0.6 - 1.2 \cdot 10^{-3}$	143	22.5	0.49	$1.39 \pm 0.20 \pm 0.33$
		$1.7 \cdot 10^{-3}$	$1.2 - 2.4 \cdot 10^{-3}$	159	8.7	0.45	$0.91 \pm 0.11 \pm 0.10$
		$4.0 \cdot 10^{-3}$	$2.4 - 7.2 \cdot 10^{-3}$	178	9.8	0.38	$0.76 \pm 0.09 \pm 0.14$

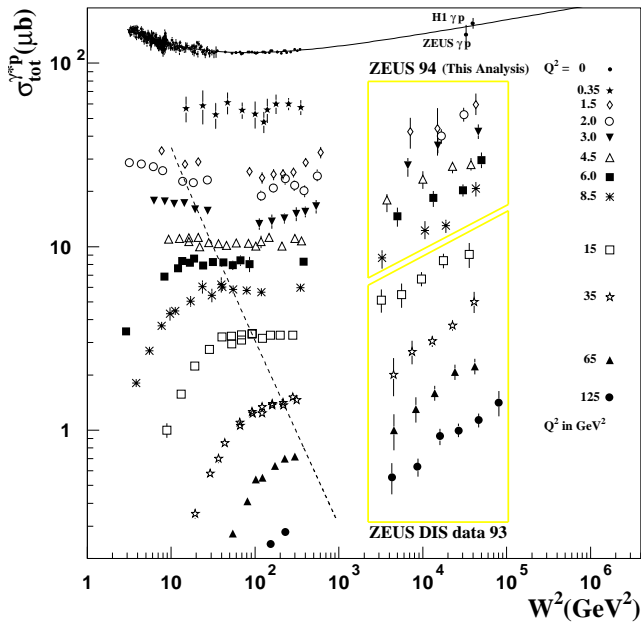


**Fig. 6.** The total virtual photon-proton cross section versus  $W^2$  for different  $Q^2$  values. The cross section values obtained from the  $F_2$  values described in this paper and the  $F_2$  values from the 1993 data [1] are shown in addition to data from previous low energy experiments [36]. The region to the right of the dashed line correspond to  $x < 1/(2m_p R_p)$ . Also shown is the  $W^2$  behaviour of the measured cross section for real photoproduction together with the prediction of Donnachie and Landshoff [37] (solid line)

The DIS cross section can be expressed as the product of the flux of virtual photons and the total cross section  $\sigma_{tot}^{\gamma^*p}$  for the scattering of virtual photons on protons [34].  $\sigma_{tot}^{\gamma^*p}$  is defined in terms of the cross section for the absorption of transverse and longitudinal photons,  $\sigma_T$  and  $\sigma_L$  respectively, by

$$\sigma_{tot}^{\gamma^*p} \equiv \sigma_T(x, Q^2) + \sigma_L(x, Q^2). \quad (9)$$

The expression for  $F_2$  in terms of  $\sigma_T$  and  $\sigma_L$  is

$$F_2(x, Q^2) = \frac{Q^2(1-x)}{4\pi^2\alpha} \frac{Q^2}{Q^2 + 4m_p^2 x^2}$$

$$\times [\sigma_T(x, Q^2) + \sigma_L(x, Q^2)], \quad (10)$$

where  $m_p$  is the mass of the proton. The separation into the photon flux and cross section can be interpreted in a way similar to the interaction of real particles provided that the lifetime of the virtual photon is large compared to the interaction time, or  $x \ll 1/(2m_p R_p)$  where  $R_p \approx 4 \text{ GeV}^{-1}$  is the proton radius [35]. At small  $x$  the expression can be written in terms of the total virtual photon-proton centre-of-mass energy  $W$  (where  $W^2 = m_p^2 + Q^2(1/x - 1)$ ) to give

$$\sigma_{tot}^{\gamma^*p}(W^2, Q^2) \approx \frac{4\pi^2\alpha}{Q^2} F_2(x, Q^2). \quad (11)$$

The measured  $F_2$  data are converted to the total virtual photon-proton cross section and shown in Fig. 6 along with low energy data and real photoproduction cross section measurements. The DIS data are seen to rise steeply as a function of  $W^2$  between the fixed target and the HERA energy range, even at  $Q^2$  values as low as  $Q^2 = 2.0 \text{ GeV}^2$  in contrast to the cross section for real photons which exhibits only a slow rise from the fixed target data to the HERA data [3, 4].

In summary, the proton structure function  $F_2(x, Q^2)$  has been measured in DIS in a new kinematic range down to  $Q^2 = 1.5 \text{ GeV}^2$  and  $x = 3.5 \times 10^{-5}$ . The GRV(94) predictions, which are based on perturbative QCD, are found to be consistent with the data. The Regge predictions of Donnachie and Landshoff based on the soft pomeron are ruled out for  $Q^2 \geq 2 \text{ GeV}^2$  and disfavoured for  $Q^2 = 1.5 \text{ GeV}^2$ . For the centre-of-mass energies between the fixed target regime and the HERA energy range, the total virtual photon-proton cross section  $\sigma_{tot}^{\gamma^*p}$  is found to rise steeply with the centre-of-mass energy for  $Q^2$  as low as  $2.0 \text{ GeV}^2$ .

*Acknowledgements.* The strong support and encouragement of the DESY Directorate has been invaluable. The experiment was made possible by the inventiveness and the diligent efforts of the HERA machine group. The design, construction and installation of the ZEUS detector have been made possible by the ingenuity and dedicated efforts of many people from inside DESY and from the home institutes who are not listed as authors. Their contributions are acknowledged with great appreciation.

## References

1. ZEUS Collab., M. Derrick et al., Phys. Lett. B316 (1993) 412; ZEUS Collab., M. Derrick et al., Z. Phys. C65 (1995) 379.
2. H1 Collab., I. Abt et al., Nucl. Phys. B407 (1993) 515; H1 Collab., T. Ahmed et al., Nucl. Phys. B439 (1995) 471.
3. ZEUS Collab., M. Derrick et al., Phys. Lett. B293 (1992) 465; ZEUS Collab., M. Derrick et al., Z. Phys. C63 (1994) 391.
4. H1 Collab., T. Ahmed et al., Phys. Lett. B299 (1992) 374; H1 Collab., S. Aid et al., DESY 95-162 (1995).
5. ZEUS Collab., M. Derrick et al., Phys. Lett. B345 (1995) 576.
6. H1 Collab., S. Aid et al., Phys. Lett. B354 (1995) 494.
7. For recent reviews, see for example:  
S. Catani, Proceedings of "Les Rencontres de Physique de la Vallée d'Aosta", ed. M. Greco, La Thuile, Italy, 6-14 Mar. 1994, Editions Frontieres (1994);  
E.M. Levin, A.D. Martin, Proceedings of the "International Workshop on DIS and Related Subjects", ed. A. Levy, Eilat, Israel, 6-11 Sept. 1994, World Scientific (1994).
8. ZEUS Collab., The ZEUS Detector, Status Report 1993, DESY 1993.
9. M. Derrick et al., Nucl. Inst. Meth. A309 (1991) 77; A. Andresen et al., Nucl. Inst. Meth. A309 (1991) 101; A. Bernstein et al., Nucl. Inst. Meth. A336 (1993) 23.
10. C. Alvisi et al., Nucl. Inst. Meth. A305 (1991) 30.
11. N. Harnew et al., Nucl. Inst. Meth., A279 (1989) 290; B. Foster et al., Nucl. Phys. B (Proc. Suppl.) 32 (1993) 181; B. Foster et al., Nucl. Inst. Meth., A338 (1994) 254.
12. J. Andruszków et al., DESY 92-066 (1992).
13. W.H. Smith et al., Nucl. Inst. Meth. A 355 (1995) 278.
14. GEANT 3.13: R. Brun et al., CERN DD/EE/84-1 (1987).
15. K. Kwiatkowski, H. Spiesberger and H.-J. Möhring, Proceedings of the Workshop "Physics at HERA" vol. 3, DESY (1992) 1294.
16. Y. Azimov, Y. Dokshitzer, V. Khoze, S. Troyan, Phys. Lett. B165 (1985) 147; G. Gustafson, Phys. Lett. B175 (1986) 453; G. Gustafson, U. Pettersson Nucl. Phys. B306 (1988) 746; B. Andersson, G. Gustafson, L. Lönnblad, U. Pettersson Z. Phys. C43 (1989) 625.
17. L. Lönnblad, Comp. Phys. Comm. 71 (1992) 15; L. Lönnblad, Z. Phys. C65 (1995) 285.
18. T. Sjöstrand and M. Bergtsson, Comp. Phys. Comm. 43 (1987) 367.
19. ZEUS Collab., M. Derrick et al., Z. Phys., C59 (1993) 231; ZEUS Collab., M. Derrick et al., Phys. Lett. B338 (1994) 483.
20. ZEUS Collab., M. Derrick et al., Phys. Lett. B315 (1993) 481.
21. ZEUS Collab., M. Derrick et al., DESY 95-093 (1995).
22. A.D. Martin, W.J. Stirling and R.G. Roberts, Phys. Rev. D50 (1994) 6734.
23. A.D. Martin, W.J. Stirling and R.G. Roberts, Phys. Rev. D51 (1995) 4756.
24. H.-U. Bengtsson and T. Sjöstrand, Comp. Phys. Comm. 46 (1987) 43; T. Sjöstrand, CERN TH-7112-93, (1994).
25. H. Abramowicz, E.M. Levin, A. Levy and U. Maor, Phys. Lett. B269 (1991) 465.
26. H. Abramowicz, A. Caldwell and R. Sinkus, DESY 95-054 (1995).
27. V.N. Gribov and L.N. Lipatov, Sov. J. Nucl. Phys. 15 (1972) 438, 675; L.N. Lipatov, Sov. J. Nucl. Phys. 20 (1975) 95; Yu. L. Dokshitzer, Sov. Phys. JETP 46 (1977) 641; G. Altarelli and G. Parisi, Nucl. Phys. B 126 (1977) 298.
28. M. Glück, E. Reya, and M. Stratmann, Nucl. Phys. B422 (1994) 37.
29. NMC Collab., P. Amaudruz et al., Phys. Lett. B295 (1992) 159.
30. G. Altarelli and G. Martinelli, Phys. Lett. B76 (1978) 89.
31. J. Kripfganz, H.-J. Möhring, and H. Spiesberger, Z. Phys. C49 (1991) 501.
32. M. Glück, E. Reya and A. Vogt, Z. Phys. C53 (1992) 127; M. Glück and E. Reya, Dortmund DO-TH 93/27 (1993); M. Glück, E. Reya and A. Vogt, Phys. Lett B306 (1993) 391; M. Glück, E. Reya and A. Vogt, Z. Phys. C67 (1995) 433.
33. A. Donnachie and P.V. Landshoff, Z. Phys. C61 (1994) 139.
34. L.N. Hand, Phys. Rev. 129 (1963) 1834; S.D. Drell and J. D. Walecka, Ann. Phys. (N. Y.) 28 (1964) 18; F.J. Gilman, Phys. Rep. 4C (1972) 95.
35. B.L. Ioffe, Phys. Lett. 30 (1969) 123; B.L. Ioffe, V.A. Khoze and L.N. Lipatov, "Hard Processes", North Holland (1984) p185.
36. NMC Collab., M. Arneodo et al., CERN-PPE-95-138 (1995); BCDMS Collab., A.C. Benvenuti et al., Phys. Lett. B223 (1989) 485; E665 Collab., Preliminary results presented by A.V. Kotwal at the XXXth Rencontres de Moriond, QCD and High Energy Interactions, March 1995, FERMILAB-Conf-95/046-Expt (1995); A.V. Kotwal, PhD thesis, Harvard University (1995).
37. A. Donnachie and P.V. Landshoff, Phys. Lett. B296 (1992) 227.